PNAS RESEARCH ARTICLE | APPLIED PHYSICAL SCIENCES

Inertia-induced mixing and reaction maximization in laminar porous media flows

Michael A. Chen[a], Sang Hyun Lee[a], and Peter K. Kang[a,b,1]

Affiliations are included on p. 9.

Edited by Klavs Jensen, Massachusetts Institute of Technology, Cambridge, MA; received April 9, 2024; accepted November 11, 2024

Solute transport and biogeochemical reactions in porous and fractured media flows are controlled by mixing, as are subsurface engineering operations such as contaminant remediation, geothermal energy production, and carbon sequestration. Porous media flows are generally regarded as slow, so the effects of fluid inertia on mixing and reaction are typically ignored. Here, we demonstrate through microfluidic experiments and numerical simulations of mixing-induced reaction that inertial recirculating flows readily emerge in laminar porous media flows and dramatically alter mixing and reaction dynamics. An optimal Reynolds number that maximizes the reaction rate is observed for individual pore throats of different sizes. This reaction maximization is attributed to the effects of recirculation flows on reactant availability, mixing, and reaction completion, which depend on the topology of recirculation relative to the boundary of the reactants or mixing interface. Recirculation enhances mixing and reactant availability, but a further increase in flow velocity reduces the residence time in recirculation, leading to a decrease in reaction rate. The reaction maximization is also confirmed in a flow channel with grain inclusions and randomized porous media. Interestingly, the domain-wide reaction rate shows a dramatic increase with increasing Re in the randomized porous media case. This is because fluid inertia induces complex three-dimensional flows in randomized porous media, which significantly increases transverse spreading and mixing. This study shows how inertial flows control reaction dynamics at the pore scale and beyond, thus having major implications for a wide range of environmental systems.

mixing | reactive transport | inertial laminar flows | porous media

Significance

Fluid inertia is the force that results from a fluid's momentum, and it is proportional to the fluid's velocity. Subsurface transport models typically ignore fluid inertia because porous media flows are considered slow. Contrary to this common assumption, this study presents compelling evidence that inertial recirculating flows significantly influence solute mixing and reaction rates within porous and fractured media. Through microfluidic experiments and numerical simulations, this study uncovers an optimal flow velocity that maximizes reactions in porous media. Even in laminar flows, inertial recirculating flows are shown to readily emerge and substantially alter solute mixing and reaction rates. The study extends these insights to larger, randomized porous media, revealing how inertia-induced transverse dispersion further intensifies mixing and reaction.

Pore-scale mixing is a key process that governs solute transport and chemical reaction in porous media flow systems (1–4) and shown to control a variety of environmental processes and industrial applications, such as carbon sequestration through rapid mineralization, hydrogen storage, contaminant transport, and chemical reactors (5–14). Fluid inertia is typically ignored in these studies of porous media flows because they are typically laminar and considered slow enough (1, 2, 15–17). Recent studies, however, have reported that complex flow patterns such as helical and recirculating flows readily emerge in laminar porous media flows (18–25), and fast flow paths in the subsurface are shown to govern continental-scale fate and transport of pollutants (26). Three-dimensional flow structures are known to play a fundamental role in enhancing mixing within porous media, even in the absence of fluid inertia (7, 27–29). In this study, we demonstrate that fluid inertia in the low-Reynolds-number regime can initiate or augment these three-dimensional structures, making them more prevalent across various pore geometries. Even weak inertia forces can create these complex flow patterns (30), and these weak inertial flows have been shown to strongly influence solute transport in laminar porous and fractured media flows (31–35). Such effects on solute transport indicate that mixing and reaction should also be strongly influenced by these weak inertial flows. However, the impacts of fluid inertia on mixing and reaction in laminar porous media flows remain unclear, and, in particular, experimental studies that focus on chemical reactions in weak inertial porous media flows remain limited (36, 37).

At high flow rates, it has long been known that porous and fractured media flows depart from Darcy's law resulting in a nonlinear relationship between pressure drop and flow rate (15, 38–42). However, unlike pipe flow where the transition from the laminar flow to turbulent flow is abrupt, there is a wide transition region between those two regimes in porous media flows (30, 39, 43–45). The flow regimes with increasing Reynolds number (Re) are Darcy (creeping) flow, weak (steady) inertial flow, strong (unsteady) inertial flow, and finally turbulent flow (43). The inertial transitional regime can span several orders of magnitude of Re and has become a subject of intense research for microfluidic mixer systems, where steady or unsteady inertial flow structures can be engineered to enhance

Author contributions: M.A.C. and P.K.K. designed research; M.A.C. and S.H.L. performed research; M.A.C., S.H.L., and P.K.K. analyzed data; and M.A.C. and P.K.K. wrote the paper.

The authors declare no competing interest.

This article is a PNAS Direct Submission.

[1]To whom correspondence may be addressed. Email: pkkang@umn.edu.

This article contains supporting information online at https://www.pnas.org/lookup/suppl/doi:10.1073/pnas.2407145121/-/DCSupplemental.

Published December 5, 2024.

mixing without creating fully chaotic flows (18, 46, 47). The key feature of these transitional flow regimes is that they remain laminar (either steady or periodically changing) while manifesting complex flow fields that significantly alter spreading and mixing compared to the Darcy flow regime. These weak inertial flows should regularly appear in porous media systems, including the hyporheic zone and fractured systems (19, 48–52). However, we lack mechanistic understanding of how laminar inertial flows influence mixing-induced reaction in porous media systems, and common groundwater models neglect these complexities (15, 26).

In this study, we address this knowledge gap by combining microfluidic experiments and numerical simulations using a mixing-controlled chemiluminescence reaction to understand pore-scale reactive transport in the presence of weak inertial flows. To this end, we first consider a single-pore-throat system where we vary fluid inertia by varying the injection rate and characterize the resulting flow, mixing, and reaction in detail. We observe an optimum Reynolds number that maximizes reaction rate and provide mechanistic explanation for the optimum. We then generalize those findings to more complex systems that are representative of porous and fractured media flows. This study shows that intricate flow structures that emerge in laminar inertia flows fundamentally alter the mixing and reaction dynamics, and the findings have broad implications for a variety of applications involving flow and reaction in porous and fractured media.

Results

We first present an experimental result in randomized porous media to motivate our study of how inertial flows influence mixing-induced reactions. Fig. 1*A* shows results from a microfluidics experiment where fluid with tracer was injected into the top half of a porous media, and fluid without tracer injected into the bottom. Fluid inertia was quantified using the Reynolds number (Re) given by

$$\mathrm{Re} = \frac{u_{\mathrm{inlet}} r_{\mathrm{grain}}}{\nu}, \qquad [1]$$

where r_{grain}, u_{inlet}, and ν represent the radius of a single pore grain, the average inlet velocity, and kinematic viscosity of acetonitrile, respectively (39). The particle Re is most widely used definition for Re in porous media studies (30). The flow rate was varied to control fluid inertia by adjusting u_{inlet}. Fig. 1*A* shows the mixing behavior in an inertial laminar flow at Re = 77.5, where complex tracer mixing and spreading dynamics are observed. Instead of a sharp mixing line along the boundary between the two injected fluids, complex mixing zones with vortical features emerge within the pore throats of this porous media. This should have a clear impact on any mixing-controlled reactions. Prior to analyzing mixing and reaction in complex porous media, we first consider the behaviors of flow, mixing, and reaction in single pore throats. Then, we analyze flow in a channel with grain inclusions, before finally investigating reactions in randomized porous media.

Recirculation Creates an Optimal Re that Maximizes Reaction. Microfluidic experiments and reactive transport simulations were performed to investigate the impacts of weak inertial flows observed in Fig. 1*A* on a mixing-induced chemiluminescence reaction. The reaction consists of a catalyzed peroxyoxalate chemiluminescence with acetonitrile as a solvent, which can be represented by TCPO + H_2O_2 → Product (2, 53). TCPO stands for bis(2,4,6-trichlorophenyl)oxalate, and serves as a primary reactant alongside

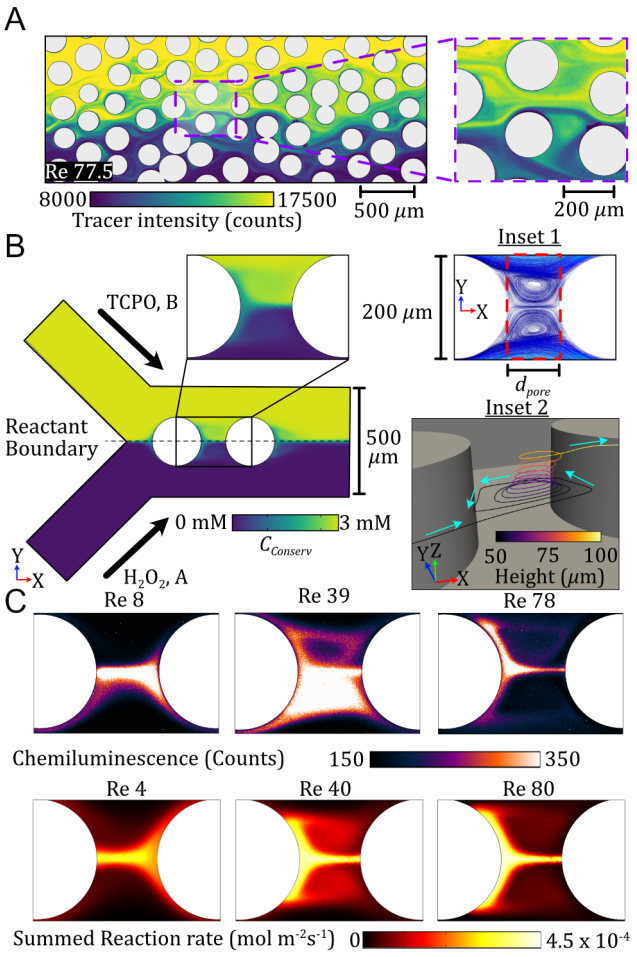

Fig. 1. Microfluidic experiments and numerical simulations reveal inertia-induced reaction maximization in laminar porous media flows. (*A*) Experimental image from a randomized porous media where fluid with fluorescent tracer is injected from the left along the top half and fluid without tracer is injected from the bottom half at a particle Re of 77.5. The image and zoomed-in image show the appearance of complex vortical structures in the tracer field. Tracer concentration is proportional to tracer intensity. (*B*) Numerical simulation of the steady-state tracer concentration field in the microchannel at Re = 40 and d_{pore} = 100 μm. The X-axis is aligned with the mean flow direction. The dashed black line shows the mixing boundary of the two reactants and aligns with the center of the channel. Inset 1: Streamlines in the pore-throat region at Re = 40 and d_{pore} = 100 μm, showing strong recirculating flows. The dashed red rectangle defines the pore-throat region for quantitative analysis, which is a cube with side lengths d_{pore} and $2r_{\mathrm{grain}}$, and depth of 100 μm. Inset 2: A single streamline entering and exiting the recirculation zone at Re = 40. The streamline is color-coded with the Z-height displaying strong Z-directional flow. (*C*) *Top*: Experimental images of chemiluminescence in a 100 μm pore throat with an exposure time of 10 s. *Bottom*: Simulation images showing the depth-averaged value of R_{Product} for the 100 μm pore throat. Microfluidic experiments and numerical simulations show a similar trend with a reaction maximization at Re = 40

hydrogen peroxides. While the catalyst concentrations can be tuned to adjust the reaction kinetics, they were kept constant in this study. The reaction was realized by an equal flow rate injection of the two reactant fluids containing either TCPO or H_2O_2 at 3 mM concentration into a Y-shaped channel where the two reactants mix at the channel confluence (Fig. 1*B*). Microfluidic experiments and numerical simulations were performed on a channel containing a single pore-throat, representing the fundamental unit of a porous media. By changing injection flow rates, the experiments and simulations considered a range of Re values from 0.4 to 100, which covers Darcy to weak inertial flow regimes, as confirmed by the steady behavior of the flow fields (43). This range corresponds to

inlet velocities ranging from 0.17 to 43 cm/s. We confirmed that both the flow and concentration fields reach steady state.

Fig. 1*B* shows the depth-averaged concentration of a conservative tracer injected from the upper inlet from simulation, calculated as $C_{conserv} = C_{TCPO} + C_{product}$ on the basis of reactant mass conservation. The interface between the two reactants, defining the reactant boundary, is a critical feature in this system and is highlighted in Fig. 1*B* with a dashed black line. Fig. 1*B* presents two important observations about this system: 1) 3D recirculating flows appear in the space between the circular pillars (pore throat region), and they are symmetric about the reactant boundary, as shown in Inset 1 of Fig. 1*B*. 2) The spatial distribution of reactants in the pore throat is clearly affected by recirculating flows, suggesting recirculation flows will affect mixing and reactant fluxes across the reactant boundary. From these observations, we expect the reaction to be strongly influenced by recirculating flows because they alter mixing and spreading of reactants (54). Inset 2 of Fig. 1*B* shows a single streamline entering and exiting the 100 μm pore throat at Re = 40, which indicates how the recirculating flow is both 3D and also advectively connected to the main flow. The streamline clearly shows a diverging spiral saddle topology that does not cross the dividing surface (the reactant boundary); thus, flux of reactants across the reactant boundary should be constrained to diffusion, which will be strongly affected by the residence time of reactants in the recirculating zones. The 3D flow topology also explains how this flow can manifest recirculation while maintaining a flow connection to the main channel flow: Flow enters near the middle depth of the channel (Z = 50 μm) and is then funneled to the top or bottom of the channel. In contrast to 2D recirculating flows that do not have flow connections to main channel flows (35, 55, 56), this flow structure has a flow connection to main channel flows. Furthermore, this differs from the flow topology following a single pillar (pore grain), where the flows are helical, creating vertical mixing and stirring, but the mean flow direction remains aligned with the flow direction in the channel (18). This contrasts with the recirculation flows observed here, where recirculation creates strong vertical flows. In porous media, pore throat regions formed by two grains are typical, and the results show that 3D recirculating flow with spiral saddle topology can readily emerge in inertia laminar regimes, which may greatly affect reaction dynamics.

The Fig. 1*C* shows how changing Re (and the emergence of spiral saddle flow) changes the spatial patterns of reaction rate. For experiments, the reaction rate is calculated from the depth summed chemiluminescence intensity, while for simulations, $R_{product}$ is directly calculated from steady-state reactant concentration fields (*Materials and Methods*). The images of the experiment and simulation match well and cross-validate each other. The pattern of the reaction in the pore throat changes dramatically when the inertial recirculation flow emerges at Re ≈ 15 (*SI Appendix*, Fig. S1). Below this value, the reaction is confined to the reactant boundary with a band of enhanced reaction at the front side of the second pillar. At Re ≈ 40, the effect of recirculating flows is clearly observed, creating reaction hotspots and shifting the enhanced reaction band to the back of the first pillar. This shift results from the recirculation flow reversing the flow direction near the reactant boundary, as shown in inset 2 of Fig. 1*B*. At Re ≈ 80, the spatial reaction pattern is similar to that of Re ≈ 40, but with significantly reduced reaction rates inside the pore throat. The zone of reaction becomes thinner and focused along the reaction boundary (i.e., the center of the pore throat). This is reasonable, as the increasing Re results from an increasing flow velocity, which therefore is also increasing the relative timescales of diffusion and advection (Péclet number). Both the experimental images and simulations show that the most overall reaction appears to occur at Re ≈ 40, where the recirculation flow appears to expand the region where reaction occurs. These results show that recirculating flows clearly have dramatic effects on mixing-induced reactions and such effects are sensitive to Re.

To quantify the inertia effect on mixing-induced homogeneous reaction, the total reaction rate was calculated at each Re for both simulations and experiments. This was calculated by spatially summing the reaction rate values observed in the pore throat and normalizing to the maximum value of that sum observed over all Re (Fig. 2*A*). The trend in normalized reaction matches well for simulations and experiments, both showing a maximum amount of reaction at Re = 40 and confirming the spatial reaction trends observed in Fig. 1. Because the results may vary with pore throat size, further experiments and simulations were performed using cases with d_{pore} = 25 μm (Fig. 2*A*) and 50 μm (*SI Appendix*, Fig. S2). These smaller pore throats also manifested an optimal Re number, but at a smaller Re. We introduced a modified Re number that incorporates porosity, given as $\tilde{\mathrm{Re}} = \frac{u_{\mathrm{inlet}} r_{\mathrm{grain}}}{\nu\phi}$. Porosity ($\phi$) is defined as the volume fraction of pore space within the area shown in the inset of Fig. 1*B* (*SI Appendix*, Table S1 and *SI Appendix* for further explanation). The reasoning is that the particle Re required to initiate inertial recirculation increases with larger porosity. We confirmed that the critical Re that initiates inertial recirculation is smaller for smaller porosity. As shown in the inset of Fig. 2*A*, incorporating porosity into the Reynolds number definition allowed us to collapse the Re vs. reaction rate curves for all three pore sizes, with the optimal Re number ($\tilde{\mathrm{Re}}$) around 75. Further study is warranted to confirm the general applicability of the modified Reynolds number.

Inset images in Fig. 2*B* illustrate the influence of fluid inertia and pore geometry on flow topology. While both cases manifest clear recirculation flows, there are some distinctive differences. Unlike d_{pore} = 100 μm case, recirculation flows are present even at a low Re number (Re ≈ 1) for the d_{pore} = 25 μm case. The noninertial recirculation in the small pore throats is consistent with observations of Stokes recirculation or laminar vortices at the pore scale (21, 24, 57). As Re increases, inertial recirculation emerges for the d_{pore} = 25 μm case, but a pair of Stokes recirculation is still present at the center of the pore throat. These are delineated by arrows in Fig. 2*B*. Unlike the inertial recirculation, these Stokes recirculation zones are advectively disconnected from the main channel. The appearance of inertial recirculating flows at moderate Re is consistent with previous studies of inertial flows at the pore scale (19, 36, 37). The changes in flow topology with these different geometries should have a significant impact on the behavior of solutes. Where the larger pore throat shows advective connections between the main flow and the pore throat, the Stokes recirculation in smaller pore throats is isolated and only accessible via diffusion, hence mixing and reaction may be hindered. These differences in topology should be an important factor in the reason for the optimal Re number.

A key factor for determining reaction rates should be the solute residence time in the pore throat, and changing flow topology should alter the residence times of solutes in the pore-throat region, where inertial recirculation could increase how long solutes reside in the pore throat. Thus, to quantify how the changes in flow topology impact solute transport, the fluid mean residence time, τ_{MRT}, in the pore throats was calculated from simulation streamlines generated in COMSOL. The streamlines were seeded in the pore throat region control volume (Fig. 1*B*), and the travel

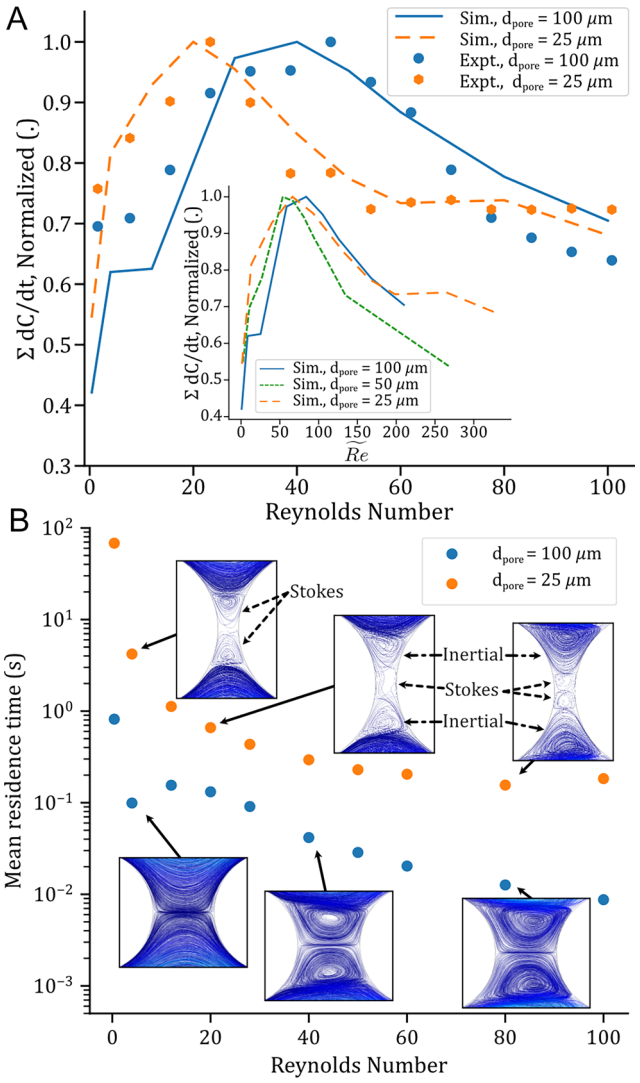

Fig. 2. Reaction rate and residence time as a function of Re for different pore-throat sizes. (*A*) Plot showing the sum of reaction rate values in the pore throat for simulations and experiments in the pore throat space defined in Fig. 1*B*. The error of the normalized intensity is approximately ~5% for any given experimental point. The reaction rates are normalized to the maximum observed in each geometry. In both pore-throat sizes, an optimal Re that maximizes reaction rate is observed, and experiments and simulations show consistent results. The inset shows the plot of simulated cases with 100, 50, and 25 μm pore throats of summed reaction rate values against the modified Re, which accounts for porosity. Further results from the 50 μm pore throat simulations are in *SI Appendix*. (*B*) Plot showing the impact of inertial recirculation on fluid residence times for the two pore throats. Residence times are calculated using streamlines seeded in the pore throat region. Images of streamlines at different Re are included as insets. Arrows with dashed lines indicate different recirculation flow structures in d_{pore} = 25 μm streamline images. The values of u_{inlet} at the optimal Re for the 100 μm (Re = 40) and 25 μm (Re = 20) cases are 17 cm/s and 8.6 cm/s, respectively. The corresponding average pore throat velocities for those two cases are 2 cm/s and 0.6 cm/s.

time along each streamline was calculated by integrating over the streamline. The resulting travel times were then averaged to obtain τ_{MRT} (*SI Appendix* for details). Fig. 2*B* shows a plot of τ_{MRT} in the two pore throat sizes considered. The 100 μm pore throat shows an initial decrease followed by an increase in residence time at Re ≈ 15, coincident with the appearance of inertial recirculation in streamline images. Streamline images demonstrate how recirculation increases fluid path length, contributing to a longer residence time. As Re further increases, the residence time decreases. This is because the velocity within the inertial recirculation increases as Re further increases. Unlike the 100 μm pore throat case, the 25 μm pore throat case shows a monotonic decrease in the residence time, which is reflective of the differences in flow topology observed in the images of the streamlines for the two different pore throats. Inertial recirculation has a clear impact on the flow behavior observed in the 100 μm pore throat case, as seen in the jump in residence time near Re ≈ 15, while a similar jump is not observed in the 25 μm pore throat. This is because the interior Stokes recirculation is present across all Re. The mean residence time plateaus as inertia recirculation occurs, but the effect is not strong enough to reverse the trend. The fact that both pore throats manifest an optimal Re despite these differences in topology and residence time is intriguing and worth further investigation.

The persistence of an optimal Re in terms of reaction rate must be the result of the competition between the fundamental processes of advection, diffusion, and reaction. We connect these processes to the observed reaction rates through three key measures. The first is "reactant availability," which is defined as the total amount of solute (or reactant amount without consumption) within the control volume and sets the maximum reaction potential. At a steady state, "reactant availability" is equivalent to reactant influx into the control volume multiplied by the averaged residence time in the control volume. The second is "mixing state": Once the reactants travel across the reactant boundary, they must mix with the other component in order for the homogeneous reaction to proceed. While mixing is ultimately accomplished by diffusion, recirculation may enhance spreading, leading to enhanced mixing and subsequently higher reaction rates (1, 18, 36, 37, 54). The last is "reaction completion," which refers to how much reaction occurred relative to what was available in the control volume (i.e., reactant availability). Reaction completion should be determined by the relative timescales of transport and reaction (Dahmköhler number). At steady state and considering no other effects (i.e., mixing and reactant availability), the reaction rate observed in the pore throat will be inversely proportional to the reaction completion. This is because the reaction rate is determined by the concentration of the reactants, which approaches zero in the case of full reaction completion. We quantify these three measures, reactant availability, mixing, and reaction completion, to explain the optimal Re.

Reactant Availability, Mixing, and Reaction Completion Create an Optimal Re. To understand the optimal Re, we trace the journey of one of the reactants (TCPO) as it enters the pore throat, mixes with the other reactant (H_2O_2), and then reacts. Given the close values of diffusion coefficient for TCPO and H_2O_2 and the symmetric injection condition, the behavior of H_2O_2 should be similar. The first step in this journey results from TCPO crossing the reactant boundary, which can be quantified by the reactant influx (mass of TCPO entering the control volume per time). The reactant influx is determined by the concentration gradient along the reactant boundary and the diffusion coefficient because diffusion is the process that ultimately brings mass across the reactant boundary. In a steady-state system without reaction, reactant inflow should be balanced by reactant outflow, so reactant availability should be equivalent to the reactant influx multiplied by the average residence time of reactants.

From this understanding, we quantify reactant availability by calculating the average tracer concentration, $\langle C_{conserv} \rangle$, within the control volume at each Re. This control volume is delineated as the dashed box in Fig. 3*A* and $\langle C_{conserv} \rangle$ represents the maximum reactant available within it. $\langle C_{conserv} \rangle$ is plotted in Fig. 3*A* alongside images of $C_{conserv}$ that illustrate how the recirculation flows

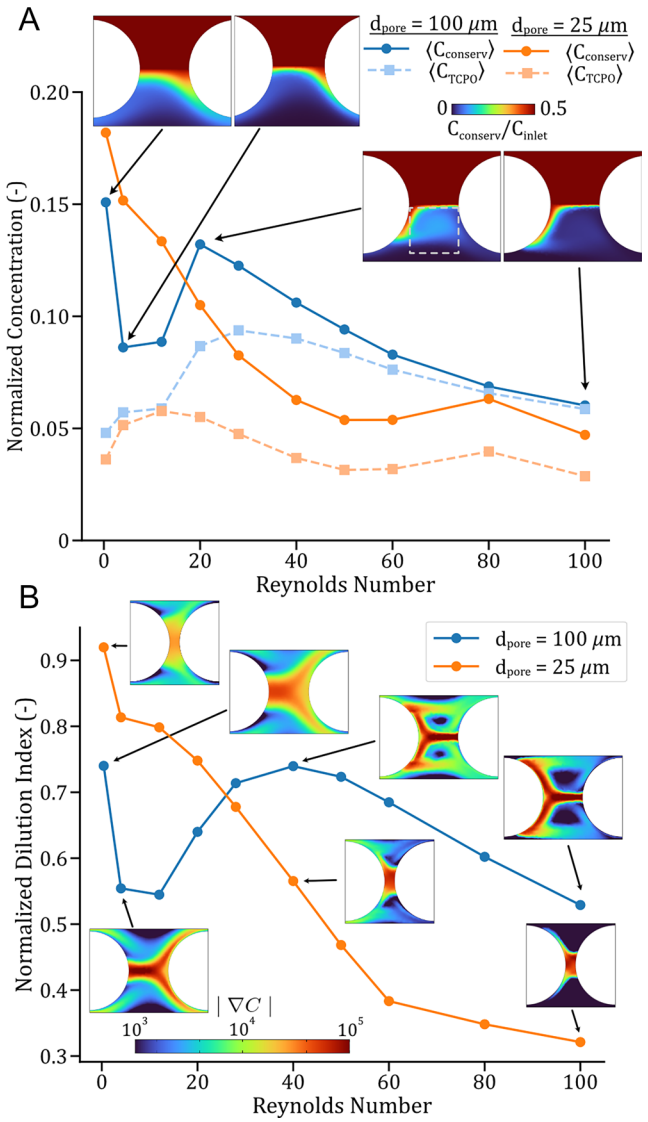

Fig. 3. Plots and images obtained from numerical simulations which explain the factors contributing to the optimal Re. (*A*) Trends in average $C_{conserv}$ and C_{TCPO} in the control volume as delineated by the dashed rectangle in an inset image as a function of Re for d_{pore} = 100 μm (blue) and d_{pore} = 25 μm (orange). The concentration values are normalized to the inlet concentration, C_{inlet}, of 3 mM. Inset images show the concentration of the tracer demonstrating the impact of recirculation on tracer spatial distributions for d_{pore} = 100 μm. Trends in $C_{conserv}$ are linked to the maximum reaction potential, while the trend of C_{TCPO} (dashed lines) shows actual reactant available after reaction proceeds. The difference between normalized $\langle C_{conserv}\rangle$ and $\langle C_{TCPO}\rangle$ is proportional to reaction completion. (*B*) Plots of the normalized dilution index as a function of Re for the two single pore throat cases considered. Inset images show the gradient of tracer concentration in the pore throat, which is proportional to the mixing rate.

alter the reactant distribution. In the case of the 100 μm pore throat, the reactant availability first decreases, then increases around when inertial recirculation initiates at Re ≈ 15, before decreasing again. The tracer images indicate the reason for these trends: Prior to the initiation of recirculation, the increase in Re is accompanied by increasing advective flows which decreases both time for diffusion across the reactant boundary and the residence time in the control volume. This is confirmed by the local Péclet number, $\mathrm{Pe} = \frac{d_{pore} r_{pore}}{D_{conserv}\tau_{MRT}}$, which initially shows a sharp increase in Pe (*SI Appendix*, Fig. S3 for details). When the inertial recirculation flow emerges at a higher Re, $\langle C_{conserv}\rangle$ increases because recirculation flow increases residence time within the control volume and also provides more time for diffusion across the reactant boundary. This suggests that the appearance of these inertial recirculation flows initially serves to enhance the reactant availability. As Re increases further, however, the Pe effect returns, reducing the reactant availability. This decrease reflects increasing pore throat flushing due to the decreasing residence time trends discussed in Fig. 2. For the 25 μm case, recirculating flows are present across the Re, and the monotonic decrease in $\langle C_{conserv}\rangle$ is mainly due to the increasing Pe effect. In *SI Appendix*, we show how the local Pe shifts from a mildly diffusive regime to an advective regime. The reactant availability trends provide information regarding the maximum reactant potential, but there are two additional processes that control the observed reaction rate.

The next step for TCPO after crossing the reactant boundary is that it mixes with the ambient fluid, containing a relative abundance of H_2O_2. Because the reactants are not well mixed in the control volume, the mixing state is an important factor that determines reaction rate. We measure mixing state by calculating the dilution index from simulation data (58). This is given by

$$E = \exp\Big(-\sum\nolimits_i p_i \log(p_i)\Big)\Delta V, \qquad [2]$$

$$p_i = \frac{c_i \Delta V_i}{\sum_i c_i \Delta V_i}, \qquad [3]$$

where c_i, ΔV_i, and ΔV represent the tracer concentration in a single element, i, the volume of that element, and the average element volume, respectively. The dilution index quantifies the degree of uniformity of the mass distribution in a control volume, and therefore, the mixing state. E is plotted in Fig. 3*B*, where it has been normalized to the value it would be under the well-mixed condition. In the 100 μm pore throat, there is an initial decrease in the mixing state, then an increase associated with the appearance of the recirculating flow up to Re = 40 before decreasing over the higher Re. In contrast, the 25 μm pore throat shows mixing decreases across the whole range of Re, similar to the trend of $\langle C_{conserv}\rangle$. Insets in Fig. 3*B* present spatial maps of $|\nabla C_{conserv}|$, which show where mixing occurs in the pore throat. In the 100 μm case, mixing state increases as recirculation flows spread out the TCPO while maintaining the concentration gradient, a feature that leads to enhanced mixing (54, 59). As Re further increases (Re > 40), the dilution index decreases, which are accompanied by a sharpening of the concentration gradients. This is due to the increase in Pe. As Pe increases, mixing by diffusion has less time to occur, leading to the decrease in mixing state. The reaction maximization around Re = 40 for the 100 μm pore throat case (Fig. 2*A*) is nicely captured by the trend in dilution index, demonstrating the importance of recirculation-induced mixing maximization in inducing reaction maximization.

To complete the journey of TCPO, we finally consider the impact of reaction completion on reaction rate, by considering the difference of average tracer concentration, $\langle C_{conserv}\rangle$, and average TCPO concentration, $\langle C_{TCPO}\rangle$. Reaction completion correlates with the difference between $\langle C_{conserv}\rangle$ and $\langle C_{TCPO}\rangle$. When $\langle C_{TCPO}\rangle$ is close to zero, this means full reaction completion leading to low reaction rate due to the lack of reactant remaining. On the other hand, if $\langle C_{conserv}\rangle$ and $\langle C_{TCPO}\rangle$ are similar, this implies low reaction completion because the reaction rate is much slower than the flushing (transport) rate in the pore throat. For this steady-state system, high reaction completion results in lower

reaction rates because there are fewer reactants remaining when the reaction is complete (*SI Appendix* for further discussion). The reaction completion trends are shown by the difference of these two measures in Fig. 3*A*. As Re increases to the optimum for each pore throat, the reaction completion decreases significantly, causing the reaction rate to increase. As Re continues to increase past the optimal Re for reaction, reaction completion stabilizes, and reactant availability and mixing trends then dominate. For the 100 μm case, it is clear that the rapid decrease in reaction completion at the lowest Re drives the observed increase in reaction rate. In the 25 μm case, the increases in reaction rate are primarily driven by the decreasing reaction completion. This is further discussed in *SI Appendix*, where the discussion based on Dahmköhler number shows how the reaction completion trends primarily contribute to the reaction rate trend at low Re, with it being less impactful at higher Re.

Thus, with the journey of TCPO complete, the explanation for the optimal Re in both pore throats is also complete. In the 100 μm case, reaction rates initially increase due to decreasing reaction completion. As Re increases, the appearance of inertial recirculation enhances both reactant availability and mixing, leading reaction enhancement up to Re = 40. However, as Re continues to increase, the decrease in residence time reduces both reactant availability and mixing, decreasing reaction rates. For the 25 μm case, the optimal Re is the result of decreasing reaction completion counterbalanced against decreases in reactant availability and mixing caused by the increasing Pe number. Because the inertial recirculation does not contact the reactant boundary for the 25 μm case, the reactant fluxes and mixing are not strongly impacted by the inertial flow. These single pore throat results highlight the intricate dance of advection, diffusion, and reaction, which is ultimately controlled by geometry-dependent recirculating flows and leads to the optimal Re number for reaction maximization.

Previous studies of chemical reaction in the presence of inertial recirculation flows have also explored how these complex flow structures may alter trends in reaction (36, 37). A study on mixing-induced reaction at flow intersections reported only reaction enhancement with increasing Re (36). Because of similarities in the reactant injection condition, we anticipate an optimal Re exists beyond the range of Re studied in that work. A separate study also reported mixing enhancement by inertial recirculation, though the observed optimal behavior was from reaction blowout by the autocatalytic reaction used, rather than the reductions of mixing and reactant fluxes observed here (37). This study demonstrates reaction maximization by inertial recirculation in porous media systems. To test the generality of optimal reaction behavior in porous media systems, we investigate systems with different pore structures.

Generalization to Randomized Porous Media. To broaden the understanding of how fluid inertia influences mixing-induced reactions in porous media systems, we extend the findings to different geometries (see details in *SI Appendix*). First, a 500 μm wide, 5 mm length channel with grain inclusions is considered (Fig. 4*A*), which mimics a fracture containing gouges or proppants. Geologic fractures are often filled with granular materials, and the appearance of inertial recirculation flows around those blockages may drive overall reaction enhancement in the channel. Images of chemiluminescence observed at a few representative Re numbers clearly show the appearance of the inertial recirculating flows in individual pore throats through the emergence of local reaction hotspots. Because the pore throat arrangement is no longer symmetric, the reaction images also show that the reactant boundary deviates from the centerline of the channel. Given

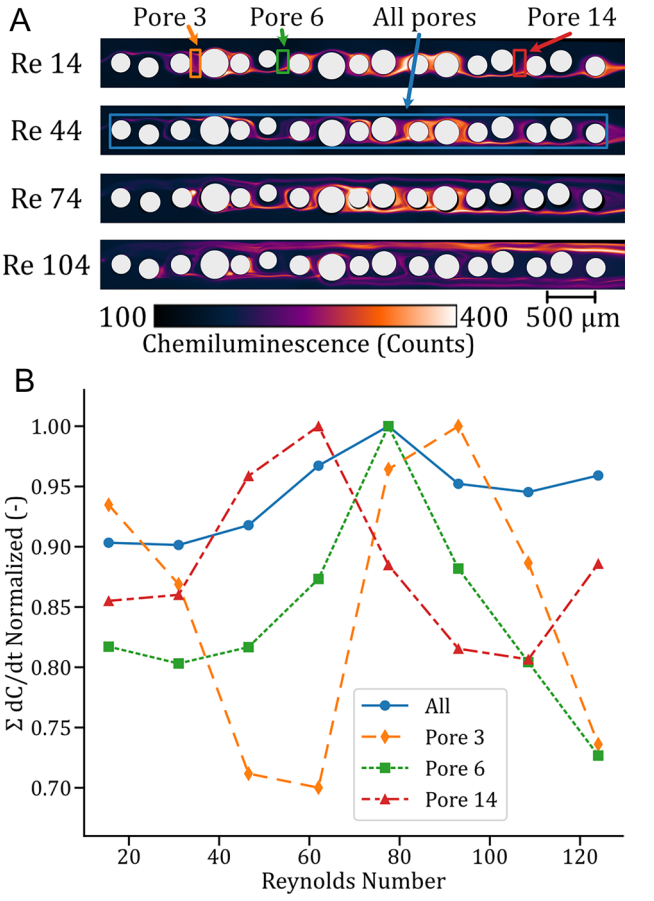

Fig. 4. Experimental results from a fracture containing grain inclusions. (*A*) Experimental images of chemiluminescence reaction in series of randomized pore throats in a fracture analog. Pillar sizes and placements of the center pore grains are randomized relative to the average r_{grain} and d_{pore} of 100 μm to maintain comparison to the single pore throats. 100 μm is the length scale used to calculate Re. (*B*) Normalized reaction rates, calculated by summing the total reaction rate over the spaces as defined in Fig. 4*A*, corresponding to single pore throats or the entire porous media region. Reaction maximization is observed in all cases.

the sensitivity of recirculation flow behavior to pore geometry, the variability in shape, location, and Re at which recirculation appears is not surprising, and the observation reinforces that inertial recirculation can readily appear in fracture flows (36, 52).

Fig. 4*B* shows quantitative trends in the amount of reaction in various control volumes as a function of Re number, either in a single pore throat or all pore throats. All control volumes considered have an optimal Re that maximizes reaction rate, and the specific optimal Re value varies depending on the control volume under consideration. These trends can be readily explained by the same framework of reactant availability, mixing, and reaction completion used to understand the single pore throat. Inertial recirculation flows enhance reactant availability and mixing, which are further magnified by deviations of the reactant boundary from the channel centerline. The channel has multiple pores, so the dynamics at upstream pores will affect reactant availability, mixing, and reaction completion at downstream pores, altering the optimal Re value. Also, a higher volume fraction compared to the single throat case may have contributed to the higher optimal Re compared to the single pore cases. The fact that the optimal Re persists in this more complex domain suggests that this optimal behavior is not restricted to single pore throats.

As a final step, we performed experiments in a wider, randomized porous media, where the porous media domain has a 2 mm width and 7 mm length from inlet to outlet. Conservative

tracer experiments were first performed to examine trends in the reactant availability and mixing state. Fig. 5*A* shows experimental tracer images, where the top half of the channel was infused with conservative tracer, along with the channel geometry. As with the other geometries considered, the concentration field at each Re reached a steady state. Tracer concentration fields at Re = 0.03 and Re = 4 show the impact of Pe number observed in single pore throats, where the concentration gradient along the reactant boundary sharpens with increasing Re (Pe effect). However, at Re ≈ 19 and higher, inertial recirculations emerge and induce mixing enhancement and transverse spreading. This enhancement is quantified by calculating the normalized dilution index in the region where the two fluids interact (named the "reaction band") (Fig. 5 *A* and *B*). The trend shows there is indeed an initial decrease in dilution index followed by a monotonic increase in dilution index as Re increases. The decrease matches with the sharpening concentration gradients observed, while the overall increase indicates that there is enhancement of mixing due to the inertial flows. There appears to be significant enhancement in mixing due to inertia-enhanced transverse dispersion, and it counters the mixing decreases observed in the single pore throats that had resulted from pore flushing and reduced residence time. The appearance of enhanced transverse dispersion due to the interplay of fluid flow and porous media structure is well established (20, 54, 59, 60). However, the effects of inertia-induced transverse dispersion on mixing-induced reaction have not yet been investigated.

Experiments with the chemiluminescence reaction were also performed in the randomized porous media (Fig. 5*C*). The trends of normalized reaction intensity obtained near the inlet region (pink rectangle in Fig. 5*A*) as well as a single pore throat region (green dashed line in Fig. 5*C*) are shown in Fig. 5*B*. Both the single pore throat region and the inlet region show an initial decrease in reaction with Re. The pore throat manifests a local optimum of reaction at around Re = 12, and then both regions of interest show increasing reaction with increasing Re. The chemiluminescence images clearly demonstrate the emergence of local reaction maximization as a result of recirculating flows, as well as the significant increase in overall reaction especially in the transverse direction. The reason for the substantial reaction enhancement ties to the enhanced transverse dispersion that was observed in the trends of tracer, and here demonstrates that the combination of inertial flows and porous media geometry results in significant enhancements in reaction via transverse dispersion. In the larger, randomized porous media case, the decreases in reactant availability and mixing that drove much of the reaction reduction in single pore throats at high Re are countered here by the presence of the inertia-induced transverse spreading across the domain. This effect is clearly reflected in the increasing trend of the dilution index and reaction rate in the inlet region at higher Re values, as shown in Fig. 5*B*. The results confirm that fluid inertia can cause significant enhancements in mixing-induced reactions in various porous media systems and that fluid inertia can significantly alter

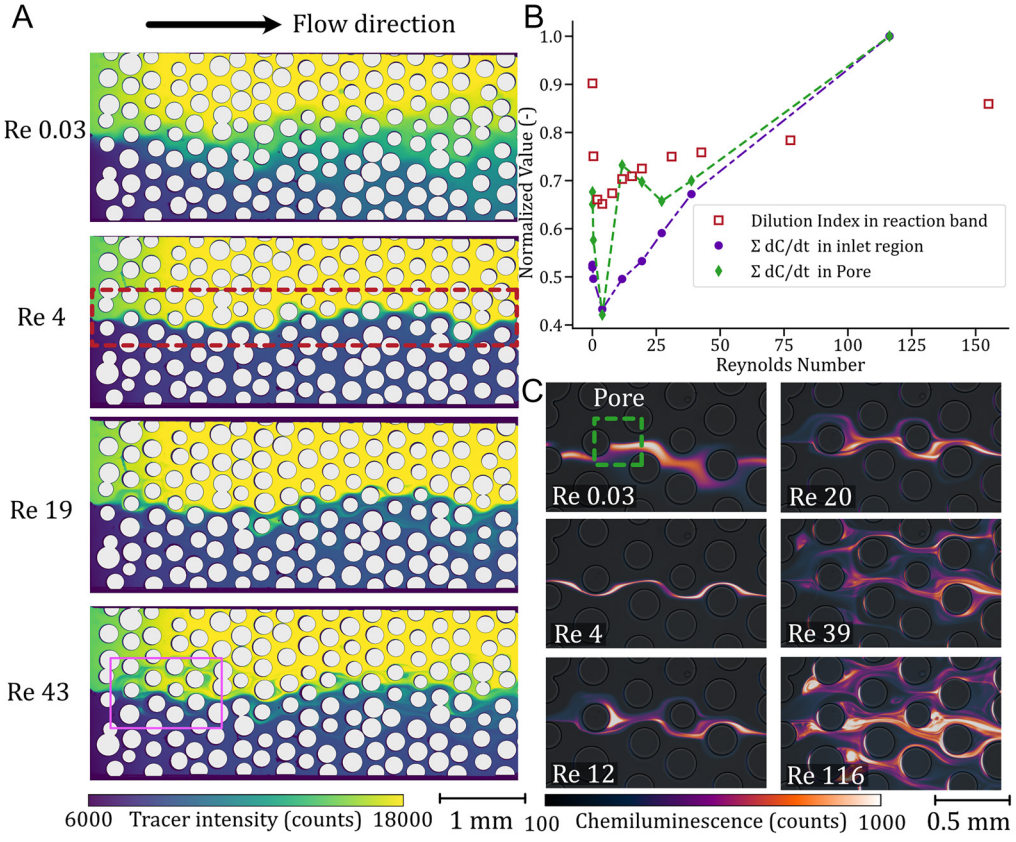

Fig. 5. Experimental results for a larger, randomized porous media. (*A*) Tracer concentration fields at various Re in the randomized porous media, showing inertia-induced transverse dispersion (Re 19 and 43). (*B*) Quantification of trends in the randomized porous media based on tracer and chemiluminescence experiments. The dilution index is measured in the region where the two fluids interact, delineated by the red dashed line (reaction band), and is normalized to the case where the concentration is uniform. The reaction intensity maps obtained from chemiluminescence experiments are used to quantify trends of reaction intensity in two different regions, normalized to the maximum value observed. The chemiluminescence region is defined either as the pore throat region shown with the green rectangle in (*C*) or the pink rectangle shown in (*A*). (*C*) Chemiluminescence images showing the trend in reaction behavior in the randomized porous media. These images demonstrate a reduction in reaction rate due to the Pe effect (Re 0.03 to 4), reaction maximization due to inertial recirculation (Re 12), and a substantial increase in reaction rate due to inertia-induced transverse spreading at higher Re.

local reaction behavior and reaction trends in larger porous media systems.

Discussion

This study clearly demonstrated that inertial recirculating flows readily occur in porous media flows and dramatically affect the mixing and transport of reactive solutes at moderate Re which can readily appear in natural and engineered porous media systems. In pore throats, 3D recirculating flows with a diverging spiral saddle topology, advectively connected to the main flow, are shown to dominate reaction dynamics by altering reactant availability, mixing, and reaction completion. In single pore throats and a channel with inclusions, this resulted in an optimal Re for reaction rates, and incorporating porosity into Re definition led to the identification of the optimal Re in single pore throats. For randomized porous media, inertia-induced transverse dispersion is identified as an additional mechanism that leads to reaction maximization. Groundwater flow models typically assume inertial flows are negligible and may underestimate the impacts of inertial flows on reactive transport. Inertial laminar flows are likely far more prevalent in both natural and engineered systems than previously assumed, especially in environments such as near pumping wells, the vadose zone, fractured aquifers or reservoirs, unconsolidated porous media, and free-flow porous media interfaces. In particular, laminar inertia flows are commonly observed in fracture flows (19, 36, 61). Therefore, the findings have wide implications for subsurface applications involving mixing and reaction in subsurface fractures. Further work is needed to understand how inertial flows manifest in porous media systems with more complex geometries. However, the relatively low Re numbers required to initiate these inertial recirculating flows suggest that this should be a common phenomenon influencing reactive transport in porous media systems, except in tight porous media.

The identified inertia effects should have a particularly significant impact on heterogeneous mineral reactions (mineral scale formation, carbon mineralization, mineral dissolution). The spiral saddle flow topology of these inertial recirculation zones, which brings flow to the top and bottom surfaces of the channel, may significantly enhance heterogeneous reactions by bringing reactants to solid surfaces and increasing surface accessibility. An important direction is to investigate how inertial recirculating flows and inertia-induced transverse spreading in porous media systems alter the feedbacks between mineral dissolution, precipitation, and fluid flow. A recent study indeed highlighted that fluid inertia can lead to significant increases in mixing-induced mineral precipitation in pore networks (62).

With improved understanding, inertial flows could be engineered to control fluid mixing for optimizing various applications such as micromixer systems, contaminant remediation, geothermal energy production, and in situ carbon mineralization (4, 18, 39, 63–65). In particular, inertia effects will be significant in subsurface applications involving injection and extraction wells because inertial recirculating flows will dominate reaction dynamics in the high flow rate zones near pumping wells. The engineering could be done by carefully selecting flow conditions in order to induce flow conditions that result in desired mixing and reaction. While Re generally describes the importance of inertial flows, Re alone is not enough to quantify inertia effects on mixing-induced reactions. Identifying inertial effects on mixing and reaction using upscaled measures should be considered in future work, similar to identifying nonlinear flows based on the linearity of flow rate–pressure gradient relationships (39, 43). As this study showed, pore-scale inertia effects can have a significant impact on macroscopic mixing and reaction behavior, making them important to be incorporated into continuum-scale reactive transport models.

Materials and Methods

Microfluidic Experiments. Microfluidic experiments of mixing-induced reactions were performed in polydimethylsiloxane experimental channels with 100 μm depth and prepared through standard photolithographic techniques using an SU-8 mold (66). A Cetoni Nemesys syringe pump was used to set the injection flow rate accurately. We employed a peroxyoxalate chemiluminescence reaction, which involves mixing two acetonitrile mixtures (A and B) to realize a mixing-induced reaction (2, 53). Mixture A contained 3 mM H_2O_2, 1.5 mM DBU, 15 mM 1,2,4-triazole, and 150 μM 3-AFA, and mixture B contained 3 mM TCPO. Mixture B was prepared and used within 48 h, while mixture A was freshly prepared and used within 25 min; the light intensity decreased if used over a longer period. The reaction is represented as H_2O_2 + TCPO Product, where the other components of mixture A are catalysts that tune reaction kinetics (2). Mixture A was injected into one side of the Y channel, and mixture B into the other; this results in light emission when the two reactants are mixed, whose intensity is proportional to the reaction rate (2, 53). FIJI was used to analyze images from experiments and stitch images of devices that were larger than a single field of view (67, 68). The light emitted from this reaction was measured in a dark room using a Nikon Ti-2E microscope with a 10× objective (NA = 0.5) or 2× objective (NA = 0.06) and a Hamamatsu ORCA Flash-4.0 scientific camera. The relative error of the measured summed intensity is approximately 5%, entirely deriving from variations in the camera sensor, as determined through steady-state mixing experiments with a known geometry. Tracer experiments were also performed using two acetonitrile mixtures, one containing 150 μM 3-AFA, and the other, pure acetonitrile, to image conservative solute transport, which were imaged using a GFP filter cube 470 nm excitation, 525 nm emission).

Numerical Simulations. 3D numerical simulations of the chemiluminescence reaction and flow were performed using COMSOL Multiphysics (v5.4) with the Chemical Reaction Engineering module.

The model domain matched the design of the single pore throat microfluidic channel, except with shorter inlets and outlets to reduce the domain size. The inlets were left long enough to yield fully developed flows. The simulated fluid was acetonitrile (density = 787 kg/m^3; kinematic viscosity = 4.3 × 10^{-7} m^2/s). Flow fields were obtained by solving the Navier–Stokes equations, which were then used to solve for reactive transport of the components H_2O_2 (mixture A), TCPO (mixture B), and the reaction product using the advection-diffusion-reaction equation

$$\frac{\partial C_i}{\partial t} = -\nabla \cdot (uC_i) + \nabla \cdot (D_i \nabla C_i) + R_i, \quad [4]$$

where C_i represents the concentration of component i. The diffusion constant (D_i) is 3 × 10^{-9} m^2/s for H_2O_2 and 1.6 × 10^{-9} m^2/s for TCPO and the product (36). R_i represents the reaction rate of component i, where $R_{TCPO,H2O2} = -kC_{TCPO}C_{H2O2}$ and $R_{product} = kC_{TCPO}C_{H2O2}$. The reaction rate constant (k) is determined from reports of experiments of light emission conducted under well-mixed and equal reactant concentration conditions (53). Based on the assumed kinetics and the half-life of the reaction determined from previously reported experimental results (53), the reaction value of k was set to 2,000 1/s/M (*SI Appendix* for details). Experiments and numerical simulations showed the flow fields and concentration fields rapidly reach steady state; therefore, flow and reactive transport simulations were decoupled in this system to reduce computational cost. The simulation grids comprised about 5 × 10^6 tetrahedral cells.

Data, Materials, and Software Availability. Analysis scripts and data have been deposited in GitHub (69) and the Data Repository for the University of Minnesota (70). All other study data are included in the article and/or *SI Appendix*.

ACKNOWLEDGMENTS. Research supported as part of the Center on Geoprocesses in Mineral Carbon Storage, an Energy Frontier Research Center funded by the US Department of Energy, Office of Basic Energy Sciences,

under award # DE-SC0023429 (porous media studies). M.A.C acknowledges the NSF Postdoctoral fellowship award No. EAR-1952686 (single pore throat computational and experimental studies, fractured media studies). P.K.K. acknowledges the NSF under Grant No. EAR-2046015 and the American Chemical Society Petroleum Research Fund for partial support of this research. Portions of this work (chip fabrication) were conducted in the Minnesota Nano Center, which is supported by the NSF through the National Nanotechnology Coordinated Infrastructure (NNCI) under Award Number ECCS-2025124.

Author affiliations: [a]Department of Earth and Environmental Sciences, College of Science and Engineering, University of Minnesota, Minneapolis, MN 55455; and [b]Saint Anthony Falls Laboratory, College of Science and Engineering, University of Minnesota, Minneapolis, MN 55414

1. J. Heyman, D. R. Lester, R. Turuban, Y. Méheust, T. Le Borgne, Stretching and folding sustain microscale chemical gradients in porous media. *Proc. Natl. Acad. Sci. U.S.A.* **117**, 13359–13365 (2020).
2. P. de Anna *et al.*, Mixing and reaction kinetics in porous media: An experimental pore scale quantification. *Environ. Sci. Technol.* **48**, 508–516 (2014).
3. S. Atis *et al.*, Experimental evidence for three universality classes for reaction fronts in disordered flows. *Phys. Rev. Lett.* **114**, 234502 (2015).
4. P. Dijk, B. Berkowitz, Precipitation and dissolution of reactive solutes in fractures. *Water Resour. Res.* **34**, 457–470 (1998).
5. X. Chen, T. Li, H. Zeng, Z. Hu, B. Fu, Numerical and experimental investigation on micromixers with serpentine microchannels. *Int. J. Heat Mass Transf.* **98**, 131–140 (2016).
6. M. Hoffmann, M. Schlüter, N. Räbiger, Experimental investigation of liquid–liquid mixing in T-shaped micro-mixers using μ-LIF and μ-PIV. *Chem. Eng. Sci.* **61**, 2968–2976 (2006).
7. A. D. Stroock *et al.*, Chaotic mixer for microchannels. *Science* **295**, 647–651 (2002).
8. P. K. Kang, E. Bresciani, S. An, S. Lee, Potential impact of pore-scale incomplete mixing on biodegradation in aquifers: From batch experiment to field-scale modeling. *Adv. Water Resour.* **123**, 1–11 (2019).
9. P. B. Kelemen *et al.*, Rates and mechanisms of mineral carbonation in peridotite: Natural processes and recipes for enhanced, in situ CO2 capture and storage. *Annu. Rev. Earth Planet. Sci.* **39**, 545–576 (2011).
10. J. M. Matter *et al.*, Rapid carbon mineralization for permanent disposal of anthropogenic carbon dioxide emissions. *Science* **352**, 1312–1314 (2016).
11. M. Ali *et al.*, Influence of pressure, temperature and organic surface concentration on hydrogen wettability of caprock; implications for hydrogen geo-storage. *Energy Rep.* **7**, 5988–5996 (2021).
12. S. Iglauer, M. Ali, A. Keshavarz, Hydrogen wettability of sandstone reservoirs: Implications for hydrogen geo-storage. *Geophys. Res. Lett.* **48**, e2020GL090814 (2021).
13. A. S. Lord, P. H. Kobos, D. J. Borns, Geologic storage of hydrogen: Scaling up to meet city transportation demands. *Int. J. Hydrog. Energy* **39**, 15570–15582 (2014).
14. R. Trias *et al.*, High reactivity of deep biota under anthropogenic CO2 injection into basalt. *Nat. Commun.* **8**, 1063 (2017).
15. J. Bear, *Dynamics of Fluids in Porous Media* (Dover, 1972).
16. B. Bijeljic, S. Rubin, H. Scher, B. Berkowitz, Non-Fickian transport in porous media with bimodal structural heterogeneity. *J. Contam. Hydrol.* **120–121**, 213–221 (2011).
17. R. Turuban, D. R. Lester, T. Le Borgne, Y. Méheust, Space-Group Symmetries Generate Chaotic Fluid Advection in Crystalline Granular Media. *Phys. Rev. Lett.* **120**, 024501 (2018).
18. H. Amini *et al.*, Engineering fluid flow using sequenced microstructures. *Nat. Commun.* **4**, 1826 (2013).
19. S. H. Lee, I. W. Yeo, K.-K. Lee, R. L. Detwiler, Tail shortening with developing eddies in a rough-walled rock fracture. *Geophys. Res. Lett.* **42**, 6340–6347 (2015).
20. Y. Ye, G. Chiogna, O. A. Cirpka, P. Grathwohl, M. Rolle, Experimental Evidence of Helical Flow in Porous Media. *Phys. Rev. Lett.* **115**, 194502 (2015).
21. E. Crevacore, T. Tosco, R. Sethi, G. Boccardo, D. L. Marchisio, Recirculation zones induce non-Fickian transport in three-dimensional periodic porous media. *Phys. Rev. E* **94**, 053118 (2016).
22. J. Wu, D. R. Lester, M. G. Trefry, G. Metcalfe, When do complex transport dynamics arise in natural groundwater systems? *Water Resour Res.* **56**, e2019WR025982 (2020).
23. C. B. Shah, Y. C. Yortsos, Aspects of flow of power-law fluids in porous media. *AIChE J.* **41**, 1099–1112 (1995).
24. A. D. Bordoloi *et al.*, Structure induced laminar vortices control anomalous dispersion in porous media. *Nat. Commun.* **13**, 3820 (2022).
25. T. J. Ober, D. Foresti, J. A. Lewis, Active mixing of complex fluids at the microscale. *Proc. Natl. Acad. Sci. U.S.A.* **112**, 12293–12298 (2015).
26. A. Hartmann *et al.*, Risk of groundwater contamination widely underestimated because of fast flow into aquifers. *Proc. Natl. Acad. Sci. U.S.A.* **118**, e2024492118 (2021).
27. J. M. Ottino, *The Kinematics of Mixing: Stretching, Chaos, and Transport* (Cambridge University Press, 1989).
28. H. A. Stone, A. D. Stroock, A. Ajdari, Engineering flows in small devices: Microfluidics toward a lab-on-a-chip. *Annu. Rev. Fluid Mech.* **36**, 381–411 (2004).
29. H. A. Kusch, J. M. Ottino, Experiments on mixing in continuous chaotic flows. *J. Fluid Mech.* **236**, 319–348 (1992).
30. B. D. Wood, X. He, S. V. Apte, Modeling turbulent flows in porous media. *Annu. Rev. Fluid Mech.* **52**, 171–203 (2020).
31. D. Bolster, Y. Méheust, T. Le Borgne, J. Bouquain, P. Davy, Modeling preasymptotic transport in flows with significant inertial and trapping effects–The importance of velocity correlations and a spatial Markov model. *Adv. Water Resour.* **70**, 89–103 (2014).
32. J. Bouquain, Y. Méheust, D. Bolster, P. Davy, The impact of inertial effects on solute dispersion in a channel with periodically varying aperture. *Phys. Fluids* **24**, 083602 (2012).
33. A. Nissan, B. Berkowitz, Inertial effects on flow and transport in heterogeneous porous media. *Phys. Rev. Lett.* **120**, 054504 (2018).
34. D. Oettinger, J. T. Ault, H. A. Stone, G. Haller, Invisible anchors trap particles in branching junctions. *Phys. Rev. Lett.* **121**, 054502 (2018).
35. S. Yoon, P. K. Kang, Roughness, inertia, and diffusion effects on anomalous transport in rough channel flows. *Phys. Rev. Fluids* **6**, 014502 (2021).
36. S. H. Lee, P. K. Kang, Three-dimensional vortex-induced reaction hot spots at flow intersections. *Phys. Rev. Lett.* **124**, 144501 (2020).
37. T. D. Nevins, D. H. Kelley, Optimal stretching in advection–reaction–diffusion systems. *Phys. Rev. Lett.* **117**, 164502 (2016).
38. P. Forcheimer, Wasserbewegung durch Boden. *Z. Vereines Dtsch. Ingeniuere* **45**, 1782–1788 (1901).
39. Z. Zeng, R. Grigg, A criterion for non-darcy flow in porous media. *Transp. Porous Media* **63**, 57–69 (2006).
40. P. G. Ranjith, W. Darlington, Nonlinear single-phase flow in real rock joints. *Water Resour. Res.* **43**, W09502 (2007).
41. C. C. Mei, J.-L. Auriault, The effect of weak inertia on flow through a porous medium. *J. Fluid Mech.* **222**, 647–663 (1991).
42. J. S. Andrade, U. M. S. Costa, M. P. Almeida, H. A. Makse, H. E. Stanley, Inertial effects on fluid flow through disordered porous media. *Phys. Rev. Lett.* **82**, 5249–5252 (1999).
43. B. D. Wood, Inertial effects in dispersion in porous media. *Water Resour. Res.* **43**, W12S16 (2007).
44. Z. Zhang, J. Nemcik, Fluid flow regimes and nonlinear flow characteristics in deformable rock fractures. *J. Hydrol.* **477**, 139–151 (2013).
45. D. L. Koch, R. J. Hill, Inertial effects in suspension and porous-media flows. *Annu. Rev. Fluid Mech.* **33**, 619–647 (2001).
46. W. Lee, H. Amini, H. A. Stone, D. Di Carlo, Dynamic self-assembly and control of microfluidic particle crystals. *Proc. Natl. Acad. Sci. U.S.A.* **107**, 22413–22418 (2010).
47. H. Amini, W. Lee, D. D. Carlo, Inertial microfluidic physics. *Lab. Chip* **14**, 2739–2761 (2014).
48. K. R. Roche *et al.*, Turbulence links momentum and solute exchange in coarse-grained streambeds. *Water Resour. Res.* **54**, 3225–3242 (2018).
49. K. R. Roche, A. Li, D. Bolster, G. J. Wagner, A. I. Packman, Effects of turbulent hyporheic mixing on reach-scale transport. *Water Resour. Res.* **55**, 3780–3795 (2019).
50. J. S. Kim, P. K. Kang, Anomalous transport through free-flow-porous media interface: Pore-scale simulation and predictive modeling. *Adv. Water Resour.* **135**, 103467 (2020).
51. F. Boano *et al.*, Hyporheic flow and transport processes: Mechanisms, models, and biogeochemical implications. *Rev. Geophys.* **52**, 603–679 (2014).
52. S. H. Lee, I. W. Yeo, K.-K. Lee, W. S. Lee, The role of eddies in solute transport and recovery in rock fractures: Implication for groundwater remediation. *Hydrol. Process.* **31**, 3580–3587 (2017).
53. T. Jonsson, K. Irgum, Very fast peroxyoxalate chemiluminescence. *Anal. Chim. Acta* **400**, 257–264 (1999).
54. M. Dentz, T. Le Borgne, A. Englert, B. Bijeljic, Mixing, spreading and reaction in heterogeneous media: A brief review. *J. Contam. Hydrol.* **120–121**, 1–17 (2011).
55. J.-Q. Zhou, L. Wang, Y.-F. Chen, M. B. Cardenas, Mass transfer between recirculation and main flow zones: Is physically based parameterization possible? *Water Resour. Res.* **55**, 345–362 (2019).
56. W. Lee, S. Yoon, P. K. Kang, Inertia and diffusion effects on reactive transport with fluid-solid reactions in rough fracture flows. *Phys. Rev. Fluids* **8**, 054502 (2023).
57. A. M. J. Davis, M. E. O'Neill, J. M. Dorrepaal, K. B. Ranger, Separation from the surface of two equal spheres in Stokes flow. *J. Fluid Mech.* **77**, 625–644 (1976).
58. P. K. Kitanidis, The concept of the dilution index. *Water Resour. Res.* **30**, 2011–2026 (1994).
59. T. Le Borgne *et al.*, Non-Fickian mixing: Temporal evolution of the scalar dissipation rate in heterogeneous porous media. *Adv. Water Resour.* **33**, 1468–1475 (2010).
60. O. A. Cirpka, G. Chiogna, M. Rolle, A. Bellin, Transverse mixing in three-dimensional nonstationary anisotropic heterogeneous porous media. *Water Resour. Res.* **51**, 241–260 (2015).
61. S. Yoon, M. Dentz, P. K. Kang, Optimal fluid stretching for mixing-limited reactions in rough channel flows. *J. Fluid Mech.* **916**, A45 (2021).
62. W. Yang, M. A. Chen, S. H. Lee, P. K. Kang, Fluid inertia controls mineral precipitation and clogging in pore to network-scale flows. *Proc. Natl. Acad. Sci. U.S.A.* **121**, e2401318121 (2024).
63. P. Guo *et al.*, Experimental investigation on macroscopic behavior and microfluidic field of nonlinear flow in rough-walled artificial fracture models. *Adv. Water Resour.* **142**, 103637 (2020).
64. S. Ó. Snæbjörnsdóttir *et al.*, Carbon dioxide storage through mineral carbonation. *Nat. Rev. Earth Environ.* **1**, 90–102 (2020).
65. Z. Pan *et al.*, Phosphate-induced immobilization of uranium in hanford sediments. *Environ. Sci. Technol.* **50**, 13486–13494 (2016).
66. J. Friend, L. Yeo, Fabrication of microfluidic devices using polydimethylsiloxane. *Biomicrofluidics* **4**, 026502 (2010).
67. J. Schindelin *et al.*, Fiji: An open-source platform for biological-image analysis. *Nat. Methods* **9**, 676–682 (2012).
68. S. Preibisch, S. Saalfeld, P. Tomancak, Globally optimal stitching of tiled 3D microscopic image acquisitions. *Bioinformatics* **25**, 1463–1465 (2009).
69. M. A. Chen, Inertial reaction modeling analysis. GitHub. https://github.com/machen/Inertial-ReactionModelingAnalysis. Deposited 7 October 2024.
70. M. A. Chen, S. Lee, P. K. Kang, Microfluidic experiments and numerical simulations of inertia-induced mixing and reaction maximization in laminar porous media flows. Data Repository for the University of Minnesota. https://doi.org/10.13020/r573-jw75. Deposited 10 October 2024.